

# THE AQUARIUS STREAM PROGENITOR WAS NOT A GLOBULAR CLUSTER: ITS HISTORY IS FAR MORE INTERESTING

ANDREW R. CASEY<sup>1,2</sup> AND DISTINGUISHED COLLABORATORS

*Draft version December 6, 2012*

## ABSTRACT

We present a detailed dynamic and chemical analysis of 5 Aquarius stream giants observed using the MIKE spectrograph on the Magellan Clay Telescope.

*Subject headings:* Galaxy: halo, structure — Individual: Aquarius Stream — Stars: FGK-giants

## 1. INTRODUCTION

Stellar streams in the halo are relics from relatively recent minor mergers in the Milky Way. The positions and kinematics of stars within these streams are sensitive to the galactic potential. As such, they can collectively constrain the fraction and distribution of accreted matter in the stellar halo, the sub-halo mass function, as well as the shape and extent of dark matter in the Milky Way. Moreover, individual elemental abundances for stars within these streams reveal the chemodynamical evolution of the Galaxy.

Wide-field surveys have proved excellent sources for finding stellar streams. Dozens of streams reaching out up to 150 kpc in the stellar halo have been identified through photometric selections and matched-filtering techniques. However, as Helmi & White (1999) point out, these methods are only successful for identifying substructures that are sufficiently distant from the solar neighbourhood. A nearby stream within  $\sim 10$  kpc will not appear as an on-sky over-density. Such substructures would only be detectable by utilising both position and kinematic information.

It is therefore necessary to survey the kinematics of solar neighbourhood stars in order to detect nearby streams. The RAVE (Radial Velocity Experiment) began such a survey in 2003 and has observed spectra from over 500,000 stars across 17,000 deg<sup>2</sup>. RAVE candidates were photometrically selected based only on their apparent magnitude of  $9 < I < 13$ , and are therefore kinematically unbiased. The RAVE data releases have provided radial velocities (Steinmetz et al. 2006) and estimates of stellar parameters (Zwitter et al. 2008; Siebert et al. 2011) now for a subset of these observations.

Using this data, Williams et al. (2011) identified a co-moving group of nearby ( $0.5 \lesssim d \lesssim 10$  kpc) stars in the direction of the Aquarius constellation. The artefact is most apparent when examining kinematics against galactic latitude for stars within  $-70^\circ < b < -50^\circ$ . Williams et al. (2011) employed a selection criteria of  $-250 < V_{hel} < -150$  km s<sup>-1</sup>,  $30^\circ < l < 75^\circ$ ,  $J > 10.3$  and identified 15 stream candidates. The average heliocentric radial velocity of these members was found to be

$V_{HELIO} = -199$  km s<sup>-1</sup>, with a dispersion of 27 km s<sup>-1</sup>. When compared to other streams identified in the halo, this is an unusually wide kinematic dispersion. Streams are generally considered to be kinematically cold, with dispersions of  $\sigma_v < 8$  km s<sup>-1</sup>. The radial velocities outputted by the RAVE survey are described to be  $\sim 2$  km s<sup>-1</sup>, so the wide kinematic distribution appears to be real.

Williams et al. (2011) quantified the statistical significance of the Aquarius substructure with comparisons to the Besancon and Galaxia models. After populating the models, the galaxy representations were discretized in  $\Delta V_{hel}$  and  $\Delta l$  grid blocks.

There is no reason to suspect that the Aquarius stream is not a real substructure.

Given the extent of stellar debris the Sagittarius dwarf has littered in the Milky Way, it is reasonable to suspect the Aquarius stream might be Sagittarius in origin. Although the metallicities reported by Williams et al. (2011) are not dissimilar from the stream, the distances and  $V_Z$ ,  $V_\phi$  for Aquarius are quite distinct from Sagittarius. Williams et al. (2011) concluded that the newly discovered stream could not be positively associated with the Monoceros stream, Hercules-Aquila cloud, or either the Canis Major or Virgo Overdensities.

In order to investigate the Aquarius progenitor and any possible association with existing substructures, Wylie-de Boer et al. (2012) observed six Aquarius stream members with medium resolution ( $R = 25,000$ ) spectroscopy. Their data indicates the stream is chemically coherent, with a dispersion in  $[Fe/H]$  of only 0.1 dex. This minimal chemical scatter suggests that the Aquarius stream progenitor is a globular cluster, since dwarf spheroidal galaxies exhibit chemical dispersions of a dex or more.

Based on sodium and nickel abundance ratios with respect to iron, they claim the Aquarius stream chemical signatures unambiguously represent those of a globular cluster.

We seek to investigate the globular cluster origin claim made by Wylie-de Boer et al. (2012). We present a detailed chemical abundance analysis for five confirmed Aquarius stream members observed using the Magellan Inamori Kyocera Echelle spectrograph (Bernstein et al. 2003) on the Magellan telescope. Details of the observations and data reduction are outlined in the following section. The data analysis is presented in §3 and a detailed discussion of these results resides in §???. In §??? we present our conclusions and critical interpretations.

<sup>1</sup> Research School of Astronomy & Astrophysics, Australian National University, Mount Stromlo Observatory, via Cotter Rd, Weston, ACT 2611, Australia

<sup>2</sup> Massachusetts Institute of Technology, Kavli Institute for Astrophysics and Space Research, 77 Massachusetts Avenue, Cambridge, MA 02139, USA

## 2. OBSERVATIONS &amp; DATA REDUCTION

The most comprehensive sample of Aquarius stream stars is presented in the discovery paper of Williams et al. (2011). Since the globular cluster origin claim of Wylie-de Boer et al. (2012) is based from a subset of six of these stars, we targeted stars largely from this study. Four of our stars are in common with Wylie-de Boer et al. (2012). An additional star from the original Williams et al. (2011) sample, J2306265-085103, was also observed. J2306265-085103 had insufficient S/N for the RAVE pipeline to accurately determine stellar parameters, so its membership hinges on radial velocity measurements. Program stars were observed in July 2011 and we observed X standard stars observed for a separate program in March 2011. All observations were taken using the 1.0" slit, which provides a spectral resolution of  $R = 28,000$ . The exposure times for our program stars varied per star from X seconds to Y seconds to ensure a signal-to-noise in excess of 100 per pixel element at 600 nm for all stars.

The data were reduced using the CarPy pipeline. Standard flat-fielding and extraction methods were employed using 10 quartz and 10 milky frames taken at the start of each night. ThAr arc lamp exposures were taken at the start of each night to provide wavelength calibration. No telluric corrections were made as atmospheric absorption does not affect any of the transitions in our line list. Each reduced echelle order was carefully normalised using a third order spline. All normalised orders were stitched together to provide a single one-dimensional spectrum from 3800-9400 Å.

## 3. ANALYSIS

## 3.1. Radial Velocities

The radial velocity for each star was determined in a two-step method. An initial estimate of the radial velocity was ascertained by cross-correlation with a synthetic spectrum of a giant with  $T_{eff} = 4500$  K,  $\log g = 1.5$ , and  $[M/H] = -1.0$  across the wavelength range 8450 – 8700 Å. The spectrum was shifted to rest frame using this initial velocity. Velocities found from cross-correlation are typically within  $1 \text{ km s}^{-1}$  of our final published value.

With our spectrum at near-rest, we measured the equivalent widths of  $N$  lines by fitting Gaussian functions to the absorption profiles. Fitting Gaussian profiles provides us with the measured equivalent width, the full-width half-maximum of the profile, and the central wavelength. Thus, the residual radial velocity can be found from the ratio of the central and rest line wavelengths. The final radial velocity for the star is provided by the mean of these  $N$  line velocity measurements. Figure 1 shows the line velocities for HD41667 after being placed at rest using our cross-correlation velocity of  $314.4 \text{ km s}^{-1}$ . As expected, the mean offset is small ( $-0.75 \text{ km s}^{-1}$ ), and our standard deviation is  $0.79 \text{ km s}^{-1}$  from 164 line measurements. This provides us with a final measured radial velocity of  $313.7 \pm 0.1 \text{ km s}^{-1}$ . This process was repeated for all observations. The radial velocities published in Table 1 are the final values from this two-step method. Heliocentric velocities agree excellently (within  $X \text{ km s}^{-1}$ ) with previously reported literature values (Williams et al. 2011; Wylie-de Boer et al.

2012).

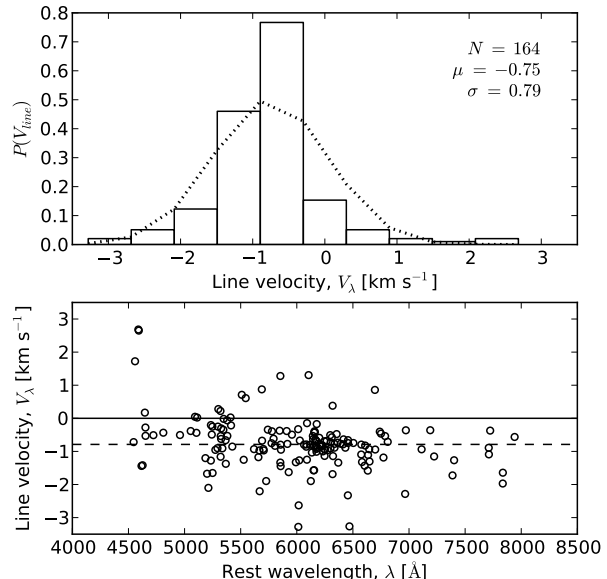


FIG. 1.— Residual velocities for each absorption line with a well-fitted Gaussian profile after correcting for the doppler shift with our cross-correlation measurement. The mean residual velocity is within our uncertainties derived from cross-correlation.

## 3.2. Line Measurements

For the measurement of atomic absorption lines, we employed the line list of Yong et al. (2005) with additional transitions of Cr, Sc, Zn, and Sr from Frebel et al. (2010). We supplemented the list with hyperfine-structure data for Sc and Mn from the Kurucz compilation ?. Molecular line data for CH was taken from ?. For lines with hyperfine structure, blended transitions or molecular features, we determined the transition abundance using a spectral synthesis approach where the abundance of a given species is found by matching a synthetic spectrum to the observed spectrum.

The equivalent widths for all transitions were measured automatically using software for this study. Given the rest wavelength and an initial guess of the FWHM, a Gaussian function is iteratively fitted to the absorption profile. At the same time, the local continuum is found within  $20 \text{ Å}$  either side of the rest wavelength using a second-order polynomial. Measuring the local continuum ensures any errors in our initial normalisation or order-stitching do not propagate through to our equivalent width measurements. Any group of pixels that deviate significantly ( $> 2\sigma$ ) to the local continuum are cosmic ray hits, or more likely trough points of a neighbouring profile. We attempt to fit a Gaussian profile to each of these groups of deviating pixels, using the best estimate of the local continuum. If a profile is successfully fitted, then all points belonging to that profile are excluded from the continuum determination. When fitting Gaussian profiles, the  $\chi^2$  difference between the observation and the profile is minimized. In order to account for blended transitions, our  $\chi^2$  function is weighted based on the distance to the rest wavelength. Pixels near the

TABLE 1  
OBSERVATIONS

Designation	$\alpha$ (J2000)	$\delta$ (J2000)	Observed Date	Airmass	Seeing (")	$t_{exp}$ (secs)	S/N <sup>a</sup> (px <sup>-1</sup> )	$V_{rad}$ (km s <sup>-1</sup> )	$V_{hel}$ (km s <sup>-1</sup> )	$V_{err}$ (km s <sup>-1</sup> )
C2225316-14437	22:25:31.7	-14:54:39.6	2011-07-30	1.033	...	...	...	-169.0	...	0.7
C2306265-085103	23:06:26.6	-08:51:04.8	2011-07-30	1.096	...	...	...	-239.3	...	0.6
HD41667	06:05:03.7	-32:59:36.8	2011-03-13	1.005	...	...	...	314.4	...	0.8
HD142948	16:00:01.6	-53:51:04.1	2011-03-14	1.107	...	...	...	6.8	...	0.4
J221821-183424	22:18:21.2	-18:34:28.3	2011-07-30	1.026	...	...	...	-170.5	...	0.5
J223504-152834	22:35:04.5	-15:28:34.9	2011-07-30	1.047	...	...	...	-180.9	...	0.7
J223811-104126	22:38:11.6	-10:41:29.4	2011-07-30	1.218	...	...	...	-248.4	...	0.7

<sup>a</sup> S/N measured at 6000 Å for each target.

rest wavelength are weighted higher than those on the wings. Although this approach relies on a reasonably accurate ( $< 4 \text{ km s}^{-1}$ ) radial velocity correction, it greatly improves the accuracy of the equivalent width measurements.

We note that the results of our iterative fitting approach are entirely insensitive to the initial FWHM guess. Increasing the initial guess from  $0.1 \text{ Å}$  to  $1$  or  $2 \text{ Å}$  – an unphysical large value for high-resolution spectra – does not alter any of our equivalent width measurements. Only a small increase in computational cost is observed. Although we are confident in our automatic equivalent width measurements, every absorption profile was examined by eye for quality.

We list the atomic data and measured equivalent widths for atomic lines used during this analysis in Table ???. Saturated lines were excluded by removing measurements with reduced equivalent widths,  $\log_{10}(EW/\lambda) > -4.5$  dex. A minimum detectable equivalent width was calculated as a function of wavelength based on the S/N, and only lines that exceeded a  $3\sigma$  detection significance were included. We have verified our equivalent width measurement techniques by comparing our measurements for 164 lines in HD140283 with the study of Norris et al. (1996). Excellent agreement is found between the two studies, which is illustrated in Figure 2. The mean difference between this study and that of ? is a negligible  $0.64 \pm 2.78 \text{ mÅ}$ , and no systematic trend is present.

### 3.3. Model Atmospheres

We employed the ATLAS9 stellar atmospheres of ? for this analysis. These one-dimensional models ignore any centre-to-limb spatial variations, assume hydrostatic equilibrium and no convective overshoot from the photosphere. Absorption lines are assumed to form under the assumption of local thermal equilibrium. The stellar parameter spacing for these grid models is  $250 \text{ K}$ ,  $0.5$  dex in surface gravity,  $0.5$  dex in  $[\text{M}/\text{H}]$  and  $0.1$  dex in  $[\alpha/\text{Fe}]$ . We interpolated the atmospheric densities, temperatures, electron pressures at all depths between stellar atmospheres using the Quickhull algorithm for this analysis. Quickhull is reliant on Delaunay tessellation, which suffers from extremely skewed cells when the grid points vary in size by orders of magnitude – as  $T_{eff}$  values do compared to  $\log g$  or  $[\text{X}/\text{H}]$ . If unaccounted for, these asymmetric cells can manifest as significant errors in interpolated densities, temperatures, pressures, and opacities across all photospheric depths. We scaled each stellar parameter between zero and unity prior to inter-

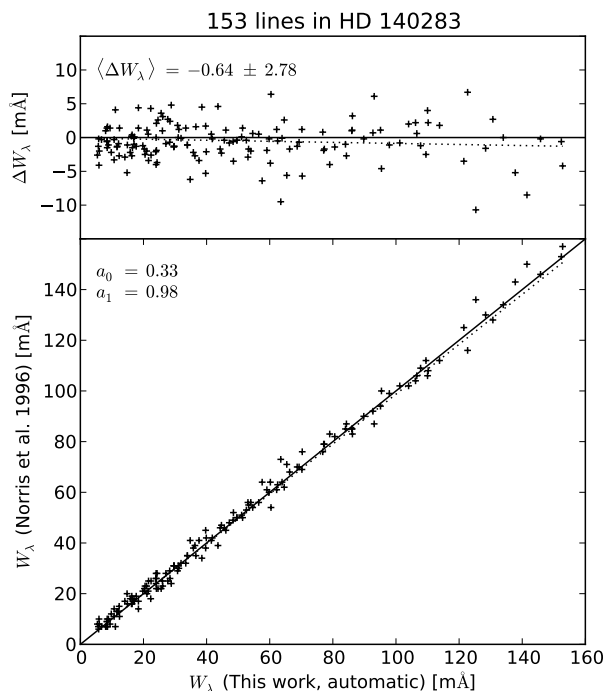


FIG. 2.— A comparison showing equivalent widths measured for HD140283 using an automatic routine (see §3.2), and those found with careful hand measurements by ?. No systematic trend is present, and the mean difference between these studies is  $\langle \Delta W_\lambda = -0.64 \pm 2.78 \text{ mÅ}$ .

polarization to minimise these errors. During this step,  $\log g$ ,  $[\text{Fe}/\text{H}]$  and  $[\alpha/\text{Fe}]$  points were scaled such that we simultaneously interpolate linearly in  $T_{eff}$  and logarithmically in all other parameters.

### 3.4. Stellar Parameters

The most recent version of the spectral synthesis code MOOG (Sneden 1973) has been used to derive individual line abundances and stellar parameters. This version employs a more accurate treatment of Rayleigh scattering (Sobeck et al. 2011), which is particularly important for transitions blueward of  $450 \text{ nm}$ . This is noteworthy, but is less relevant for this analysis as most of our line measurements are redward of  $450 \text{ nm}$ . We have scaled our abundances to solar values using the chemical composition of Asplund et al. (2009).

#### 3.4.1. Photometric Effective Temperatures

The effective temperatures published for all of our stars in Table ?? were derived spectroscopically (see §??). For consistency, we have also estimated effective temperatures using 2MASS infrared photometry. The  $J - K$  colour has been employed for these calculations because it has the least dependence on metallicity. The Aquarius stream is relatively close and at high-latitude, so significant extinction by dust is not expected. Nevertheless, the dust maps of ? have been used to estimate the effect of extinction along the line-of-sight. Two different  $T_{eff}$ -colour relationships have been used for estimating temperatures: the ? calibration for dwarfs/sub-giants, and the ? calibration for giants. All photometrically-derived temperatures are listed in ??.

### 3.4.2. Effective Temperature

The effective temperature for each star was found by demanding a zero-trend in excitation potential and abundance for each measured Fe I line. In the same way, the microturbulence was found by demanding a zero trend in reduced equivalent width against abundance. Linear relationships with slopes of  $|0.001|$  dex were considered to be converged.

### 3.4.3. Surface Gravity

Surface gravity was found by forcing the mean Fe I and Fe II abundances to be equal, whilst maintaining zero trends with the excitation potential, reduced equivalent width and abundance. After these parameters had converged, the model metallicity was exactly matched to that of our line abundances. Line abundances that were unusually deviant ( $3\sigma$ ) from the mean were removed. The largest number of outlier measurements removed for any observation was N for X.

### 3.4.4. Metallicity, $[M/H]$

Determining the stellar parameters for a given star is an iterative process. Once the effective temperature, microturbulence and surface gravity were deduced, the model atmosphere abundance was matched to our solar-scaled Fe I abundance. The degeneracy between parameters required a refinement of the stellar parameters until the line abundances were consistent with the model atmosphere.

## 3.5. Abundances

### 3.5.1. Carbon

### 3.5.2. Oxygen

Oxygen is a particularly difficult element to measure. There are only a handful of lines available in an optical spectrum: the forbidden [O I] lines at 630 nm and 636 nm, and the O I triplet lines at 777 nm. The forbidden lines are very weak, and become immeasurable in either hot and/or metal-poor stars ( $[\text{Fe}/\text{H}] \lesssim -1.5$  dex). When they are present, depending on the radial velocity of the star, the [O I] can be significantly affected by telluric absorption. Moreover, the 630 nm line is blended with a Ni I absorption line (?), and hence the region requires careful consideration. Although the O I triplet lines at 777 nm are stronger than the forbidden lines, they are extremely susceptible to NLTE and 3D effects (?), and sensitive to changes in microturbulence. ? showed that

oxygen abundances measured under the assumption of LTE in their sample are 0.08 dex higher than abundances derived from the ‘true’ oxygen content derived from the forbidden lines (?).

The [O I] lines were measurable in four of our candidates. Careful consideration was taken when correcting for telluric absorption, and we inspected all lines for any contamination by the earth’s atmosphere. The 6300Å line in one of our candidates, C2306265-085103, was sufficiently affected by telluric absorption such that we considered the line immeasurable. Thus, only the 6363Å line was used to derive an oxygen abundance for C2306265-085103. In our hottest star, J223811-104126, the forbidden oxygen lines were not detected above a  $3 - \sigma$  significance. After synthesising the region, we deduce a conservative upper limit of  $[\text{O}/\text{Fe}] < -0.50$  dex from the [O I] lines. This is consistent with the rest of our candidates, with  $[\text{O}/\text{Fe}]$  abundances varying between 0.41 to 0.57 dex.

In order to derivability an oxygen measurement for J223811-104126, we were forced to use the triplet lines at 777nm. Each line was synthesised, and a mean abundance was derived for each candidate. Abundances calculated from the oxygen triplet lines were systematically 0.27 dex higher than found from the [O I] lines. ? found  $[\text{O}/\text{Fe}]$  values based on the O I permitted triplet lines are on average  $0.19 \pm 0.07$  dex higher than those found from the forbidden lines, after NLTE corrections had been applied. They concluded the weak forbidden lines, when not too weak, probably give the most reliable estimate of  $[\text{O}/\text{Fe}]$ . Thus, our 0.27 dex offset between measurements of the [O I] and O I triplet lines is exactly the same as found by ?, which we attribute to a combination of NLTE, 3D and other systematic effects.

From the permitted O I triplet, we derive an oxygen abundance of  $[\text{O}/\text{Fe}] = 0.41 \pm 0.01$  dex (random scatter) for J223811-104126. This measurement will be systematically higher than the ‘true’ abundance if it were discernible from the [O I] lines, on the order of  $\sim 0.27$  dex. When we apply this crude offset derived from the rest of our sample, we arrive at a corrected abundance of  $[\text{O}/\text{Fe}] = 0.14 \pm 0.08$  dex for J223811-104126. This is the most oxygen-deficient in our Aquarius sample.

### 3.5.3. Sodium

Sodium is produced during hydrogen burning through the Ne-Na cycle, as well as through carbon burning in massive stars by the dominant  $^{12}\text{C}(^{12}\text{C}, p)^{23}\text{Na}$  process. The total amount of Na production by C-burning is dependent on the neutron excess of the star, which slowly increases through stellar evolution along the red giant branch. Massive stars ( $> 8M_{\odot}$ ) eventually deliver their manufactured sodium to the interstellar-medium through SN II events. Because the eventual SN II explosion is devoid of any significant beta-decay processes, the neutron excess of the exploded material is representative of the pre-explosion abundance.

The explosive material eventually condenses to form the next generation of stars, which will have a net increase in their neutron excess with respect to their predecessors. Since the Na-production rate is correlated with the neutron excess, an overall increase in the total Na and Na-production rate between stellar generations is expected. Thus, an increase in the Na abundance between

TABLE 2  
STELLAR PARAMETERS

Designation	$T_{\text{eff}}$	$\log g$	$v_t$	[Fe/H]	$T_{\text{eff}}$	$\log g$	$v_t$	[Fe/H]	Source
C2225316-14437	4350	1.60	1.80	-1.19	$4235 \pm 118$	$1.45 \pm 0.21$	$1.96 \pm 0.11$	$-1.20 \pm 0.14$	Wylie-de Boer et al. (2012)
C2306265-085103	4180	1.00	1.80	-1.16	...	...	...	...	...
HD41667	4630	1.70	1.66	-1.21	4605	1.88	1.44	-1.16	Gratton et al. (2000)
HD44007	4790	1.78	1.63	-1.80	4850	2.00	2.20	-1.71	Fulbright (2000)
HD142948	4950	2.19	1.78	-0.79	4713	2.17	1.38	-0.77	Gratton et al. (2000)
J221821-183424	4570	0.80	1.93	-1.60	$4395 \pm 205$	$1.45 \pm 0.35$	$1.96 \pm 0.18$	$-1.15 \pm 0.21$	Wylie-de Boer et al. (2012)
J223504-152834	4620	2.15	1.44	-0.65	$4597 \pm 158$	$2.40 \pm 0.14$	$1.47 \pm 0.07$	$-0.98 \pm 0.17$	Wylie-de Boer et al. (2012)
J223811-104126	5100	3.00	1.21	-1.44	$5646 \pm 147$	$4.60 \pm 0.15$	$1.09 \pm 0.11$	$-1.20 \pm 0.20$	Wylie-de Boer et al. (2012)

generations of massive stars is a natural consequence of nucleosynthesis. Sodium content also becomes important for production of Ni during the SN II event (see §??) because  $^{23}\text{Na}$  is the only stable isotope produced in significant quantities during the C- (or O-) burning stages.

We have measured the sodium content for our stars using 2-3 clean, unblen

### 3.5.4. $\alpha$ -elements (Mg, Ti, Si, Ca)

### 3.6. Distances

### 3.7. Dynamics

## 4. DISCUSSION

We seek to investigate the nature of the Aquarius stream, as well as the specific globular cluster origin claim by Wylie-de Boer et al. (2012). The stellar parameters reported in Wylie-de Boer et al. (2012) differ slightly to those found in Table ???. Wylie-de Boer et al. (2012) deduce their stellar parameters through the use of a  $\chi^2$  analysis against synthetic spectra from the Munari et al. (2005) grid. Our temperatures have been determined by forcing a zero trend in excitation potential and line abundance. In general, these temperatures agree within the uncertainties, with our temperatures being marginally (23-175 K) hotter. The only noteworthy exception is J223811-104126, where we find an effective temperature 546 K cooler than Wylie-de Boer et al. (2012). This is the largest discrepancy we see in any of our standard or program stars.

Wylie-de Boer et al. (2012) calculate microturbulence with the empirical relationships from Reddy et al. (2003) for dwarfs and ? for giants. These relationships are based upon the derived temperature and surface gravities. Our published microturbulence values agree excellently with the values presented in Wylie-de Boer et al. (2012) with the exception of J223811-104126, which we find to be a F-type giant and others have claimed is a -type dwarf from medium-resolution spectra (Wylie-de Boer et al. 2012; Williams et al. 2011). Small discrepancies in microturbulence for other stars can be directly attributed to difference in surface gravities.

### 4.1. Stellar Parameter Discrepancies with Wylie-de Boer et al. (2012)

The stellar parameter discrepancies between this study and Wylie-de Boer et al. (2012) need to be addressed. There are noteworthy differences in the stellar parameter determination between these studies. In the Wylie-de Boer et al. (2012) study, the temperature, metallicity and surface gravity were found by a  $\chi^2$  analysis

against the spectral library of Munari et al. (2005) after it was convolved and re-sampled to match the observational data. The comparison regions used for analysis were 4900-5200 Å and 5575-5725 Å. Using these parameters, an interpolated MARCS (?) model atmosphere was used to synthesise elemental abundances. Oscillator strengths in their line list were astrophysical; they were derived from a reverse analysis using the ? solar atlas. The spectrum synthesis code MOOG was used to derive abundances for individual Fe I and Fe II lines. The median abundance of Fe I lines was taken as the overall stellar metallicity, scaled using the Grevesse & Sauval (1998) solar abundances.

The study of Wylie-de Boer et al. (2012) is of slightly lower resolution ( $R = 25,000$  compared to  $R = 28,000$  presented here), but with a much lower signal-to-noise ratio:  $\sim 25$  compared to  $> 100$  per pixel element achieved here. Given the slightly lower spectral resolution and modest signal-to-noise in their study, there are fewer unblended absorption lines available. In fact, there are very few transitions present in their published line list: only 14 Fe I lines and 3 Fe II lines are available. For contrast, our metallicity determinations are based off X Fe I and Y Fe II lines. Given the metallicity of these stars, it is somewhat surprising that there were not more unblended transitions available to Wylie-de Boer et al. (2012).

With the exception of J223811-104126, we believe our stellar parameters are largely in agreement with the exception of metallicity. The Fe I abundances differ significantly for the four stars in common: 0.01 dex, -0.45 dex, 0.33 dex, -0.24 dex. In order to investigate the source of these discrepancies, we repeated our analysis for the four common stars using the line list of Wylie-de Boer et al. (2012). The results of this analysis is shown in Table ??.

One Fe I line at 6420.060 Å was not detectable in any of our stars, even though the S/N at this point exceeds 120 in every observation. Additionally, we could not identify the line in the existing VALD database.

Given the line list employed, the overall data quality and the lack of Fe I lines available for analysis, it appears the Aquarius stream stars have conspired to present a tight metallicity distribution function – suggesting of a globular cluster origin. In contrast, our high-resolution analysis suggests a significantly broader metallicity distribution of  $\langle [\text{Fe}/\text{H}] \rangle = X.XX \pm X.XX$  dex.

### 4.2. The Aquarius Stream M.D.F.

### 4.3. The Na-O Relationship

Extensive studies looking at stars in globular clusters have revealed variations in light-element abundances,

TABLE 3  
PROGRAM STAR ABUNDANCES

J221821-183424							C2225316-14437						
Species	$N$	$\log \epsilon(X)$	$\sigma_\epsilon$	[X/H]	[X/Fe]	$\sigma$	Species	$N$	$\log \epsilon(X)$	$\sigma_\epsilon$	[X/H]	[X/Fe]	$\sigma$
O I	2	7.50	0.04	-1.18	0.41	0.02	O I	2	7.90	0.01	-0.79	0.48	0.01
Na I	2	4.56	0.14	-1.68	-0.08	0.10	Na I	3	5.09	0.17	-1.15	0.12	0.10
Mg I	4	6.55	0.37	-1.04	0.55	0.18	Mg I	4	6.98	0.24	-0.62	0.65	0.12
Al I	1	5.04	0.00	-1.41	0.18	...	Al I	4	5.87	0.09	-0.58	0.68	0.04
Si I	5	6.28	0.08	-1.23	0.37	0.04	Si I	5	6.96	0.15	-0.55	0.72	0.07
Ca I	4	4.97	0.04	-1.37	0.23	0.02	Ca I	4	5.50	0.04	-0.84	0.43	0.02
Sc I	0	...	...	...	...	...	Sc I	0	...	...	...	...	...
Sc II	6	1.52	0.08	-1.63	-0.04	0.03	Sc II	5	2.05	0.13	-1.10	0.17	0.06
Ti I	0	...	...	...	...	...	Ti I	4	4.04	0.03	-0.91	0.36	0.01
Ti II	4	3.81	0.13	-1.14	0.45	0.07	Ti II	2	4.26	0.08	-0.69	0.58	0.06
V I	3	2.23	0.01	-1.70	-0.11	0.01	V I	6	2.92	0.17	-1.01	0.26	0.07
Cr I	11	3.74	0.07	-1.90	-0.30	0.02	Cr I	8	4.27	0.16	-1.37	-0.10	0.06
Mn I	3	3.29	0.04	-2.14	-0.54	0.02	Mn I	3	4.14	0.05	-1.29	-0.02	0.03
Fe I	52	5.91	0.09	-1.59	0.00	0.01	Fe I	61	6.23	0.11	-1.27	0.00	0.01
Fe II	13	5.90	0.05	-1.60	0.00	0.01	Fe II	10	6.17	0.06	-1.33	-0.07	0.02
Co I	1	3.35	0.00	-1.64	-0.05	...	Co I	3	3.92	0.12	-1.07	0.20	0.07
Ni I	5	4.61	0.15	-1.61	-0.01	0.07	Ni I	7	5.04	0.09	-1.18	0.09	0.03
Cu I	1	2.13	0.00	-2.06	-0.47	...	Cu I	1	3.35	0.00	-0.84	0.43	...
Zn I	2	3.15	0.11	-1.41	0.19	0.08	Zn I	2	3.46	0.23	-1.10	0.17	0.17

J223504-152834							J223811-104126						
Species	$N$	$\log \epsilon(X)$	$\sigma_\epsilon$	[X/H]	[X/Fe]	$\sigma$	Species	$N$	$\log \epsilon(X)$	$\sigma_\epsilon$	[X/H]	[X/Fe]	$\sigma$
O I	2	8.48	0.09	-0.21	0.46	0.07	O I	1	8.60	0.00	-0.09	1.36	...
Na I	3	5.76	0.12	-0.48	0.19	0.07	Na I	2	4.76	0.10	-1.48	-0.03	0.07
Mg I	3	7.50	0.24	-0.10	0.58	0.14	Mg I	3	6.49	0.42	-1.11	0.34	0.24
Al I	3	6.10	0.08	-0.35	0.32	0.05	Al I	2	5.10	0.14	-1.35	0.10	0.10
Si I	5	7.11	0.10	-0.40	0.28	0.04	Si I	3	6.38	0.04	-1.13	0.32	0.02
Ca I	4	6.03	0.04	-0.31	0.36	0.02	Ca I	4	5.30	0.03	-1.04	0.41	0.01
Sc I	0	...	...	...	...	...	Sc I	0	...	...	...	...	...
Sc II	6	2.70	0.14	-0.45	0.23	0.06	Sc II	6	1.75	0.14	-1.40	0.05	0.06
Ti I	4	4.63	0.02	-0.32	0.36	0.01	Ti I	0	...	...	...	...	...
Ti II	2	4.92	0.26	-0.04	0.64	0.19	Ti II	4	3.83	0.09	-1.12	0.33	0.04
V I	6	3.67	0.22	-0.26	0.41	0.09	V I	1	2.42	0.00	-1.51	-0.06	...
Cr I	7	4.94	0.09	-0.70	-0.02	0.03	Cr I	12	4.12	0.06	-1.52	-0.07	0.02
Mn I	3	5.08	0.10	-0.35	0.33	0.06	Mn I	3	3.55	0.04	-1.88	-0.43	0.02
Fe I	64	6.83	0.12	-0.67	0.00	0.02	Fe I	33	6.05	0.06	-1.45	0.00	0.01
Fe II	12	6.82	0.07	-0.68	0.00	0.02	Fe II	11	6.00	0.09	-1.50	-0.05	0.03
Co I	3	4.53	0.14	-0.46	0.21	0.08	Co I	0	...	...	...	...	...
Ni I	7	5.62	0.09	-0.60	0.08	0.03	Ni I	2	4.82	0.04	-1.40	0.05	0.03
Cu I	1	3.85	0.00	-0.34	0.33	...	Cu I	1	2.39	0.00	-1.80	-0.35	...
Zn I	2	4.17	0.03	-0.39	0.28	0.02	Zn I	2	3.17	0.04	-1.39	0.06	0.03

C2306265-085103						
Species	$N$	$\log \epsilon(X)$	$\sigma_\epsilon$	[X/H]	[X/Fe]	$\sigma$
O I	2	8.09	0.15	-0.60	0.57	0.10
Na I	2	5.25	0.00	-0.99	0.18	0.00
Mg I	2	6.84	0.07	-0.76	0.41	0.05
Al I	4	5.56	0.08	-0.89	0.28	0.04
Si I	5	6.66	0.08	-0.85	0.32	0.03
Ca I	4	5.48	0.04	-0.86	0.31	0.02
Sc I	0	...	...	...	...	...
Sc II	6	2.18	0.15	-0.97	0.20	0.06
Ti I	4	4.06	0.03	-0.89	0.28	0.01
Ti II	3	4.21	0.36	-0.74	0.43	0.21
V I	4	2.88	0.06	-1.05	0.12	0.03
Cr I	4	4.20	0.26	-1.44	-0.27	0.13
Mn I	3	4.35	0.10	-1.08	0.09	0.06
Fe I	63	6.33	0.12	-1.17	0.00	0.01
Fe II	11	6.31	0.09	-1.19	-0.02	0.03
Co I	3	4.00	0.15	-0.99	0.18	0.08
Ni I	7	5.08	0.08	-1.14	0.03	0.03
Cu I	1	3.55	0.00	-0.64	0.53	0.00
Zn I	2	3.38	0.14	-1.18	-0.01	0.10

most notably an anti-correlation in sodium and oxygen content ?. Between generations of stars within a globular cluster, the oxygen abundance is transformed into nitrogen, reducing the overall oxygen abundance. This pattern has been repeatedly demonstrated in all well-studied globular clusters, although the strength of the anti-correlation varies between systems. Even though oxygen undergoes internal mixing during its evolution along the giant branch, it is now well established that any observed abundance variations due to such mixing is limited to Li, C, and N. Therefore, the observed anti-correlations in light elements required a different astrophysical explanation.

? defined three components of stars following this abundance pattern within a population: primordial, intermediate, and extreme. The  $[\text{Na}/\text{Fe}]$  and  $[\text{O}/\text{Fe}]$  abundances for a given star defines which component it belongs to. Primordial (first-generation) stars are those with Na and O content similar to field stars of the same metallicity. For a well-studied system, stars with the lowest cluster  $[\text{Na}/\text{Fe}]$  abundances are characterised as primordial. An intermediate population – the second-generation of stars – will have super-solar sodium abundances, and demonstrate a slight depletion in oxygen content. The abundance exhaustion rate is ultimately dependent on the star-formation history of the cluster environment. The intermediate population is sub-divided based on how much the O and Na abundances depart from the primordial population: stars with  $[\text{O}/\text{Na}] > -0.9$  dex are classified as belonging to an extreme component of this Na-O pattern because they differ greatly from the primordial cluster abundance. The extreme O-depletion component has only been observed in a few clusters (more massive ones preferentially), indicating an extended star-formation history in more massive clusters.

The exact astrophysical mechanism for oxygen depletion between generations of stars in globular clusters is still under debate. However, it is clear that this trend has been well-demonstrated empirically. Several hypotheses have been proposed in order to account for oxygen depletion between stellar generations, including massive binaries (?) or fast-rotating massive stars (?). While the exact procedure is yet to be fully characterized, we can describe the abundance variation as a simple oxygen depletion (or dilution) model with time. Through comparisons with existing globular clusters, we can still draw inferences on the star-formation history of a system from measuring sodium and oxygen in a sample of its stars.

It is clear that careful consideration must be given inferring star-formation histories from observed stellar abundances. In addition to the normal care afforded for measuring elemental abundances from high-resolution spectroscopic data, attention must be given to telluric absorption, Ni contamination, and NLTE corrections when deriving oxygen abundances. Furthermore, when characterising the oxygen depletion rate – and hence the strength of the Na-O anti-correlation for a cluster – it is vital to obtain observations for stars belonging to all three components (where possible). If only a primordial sample of stars in a globular cluster is observed, then their  $[\text{Na}/\text{Fe}]$  and  $[\text{O}/\text{Fe}]$  abundances will be indistinguishable from halo stars of a similar metallicity. In such a scenario, any inferred anti-correlation could equally be

explained by intrinsic chemical scatter or observational uncertainties.

With high-resolution data and modest ( $\sim 30 \text{ pixel}^{-1}$ ) signal-to-noise, ? measured Na and O abundances for four of their six Aquarius stream members. This research has four stars in common with the ? study, but Na and O measurements exist for only three stars that are in both samples. We have measurements for all of our stars, including J223811-104126, for which we ascertained an upper limit from the  $[\text{O I}]$  lines of  $[\text{O}/\text{Fe}] < 0.5$  dex, and a NLTE-corrected abundance of  $[\text{O}/\text{Fe}] = 0.21$  (CHECK) from the O I triplet lines.

The ? measurements indicate two stars with solar-type levels of Na – identical to field star Na abundances for their metallicity – and two stars with super-solar sodium content. Combined with measurements of other light elements (see §??, ??) they claim the Aquarius stream is “consistent with a globular cluster origin”. The Wylie-de Boer et al. (2012) abundances themselves do not demonstrate a classical Na-O anti-correlation. In fact, they have a slight positive relationship: their Na-enhanced stars show an increased oxygen content, contrary to an expected oxygen depletion between generations with. However, this trend is drawn from a sample of only four stars – the same as this study if our upper limit for J223811-104126 is excluded.

#### 4.4. The Al-Mg Relationship

The Na-O anti-correlation is likely the result of complete CNO and Ne-Na cycles of proton reactions in globular cluster stars. There is also evidence in some clusters that the Mg-Al nucleosynthesis cycle is also active.

The conditions required for these reactions are significantly higher than the CNO and Ne-Na cycle: temperatures of 70 MK are required for the Mg-Al channel instead of just 25 MK for the CNO/Ne-Na cycles ?.

#### 4.5. The Na-Ni Relationship

#### 4.6. Possible Progenitors

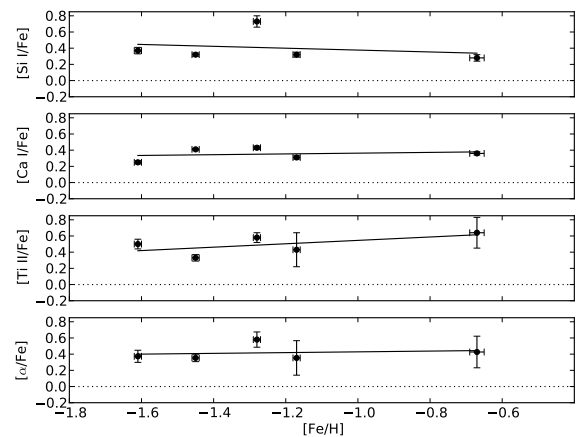


FIG. 3.— A plot showing  $[\alpha/\text{Fe}]$  for all Aquarius stream stars.

TABLE 4  
OBSERVED TARGETS

ID	$\alpha$ (J2000)	$\delta$ (J2000)	Air mass	S/N <sup>a</sup> (px <sup>-1</sup> )	$V_{\text{helio}}$ (km s <sup>-1</sup> )
HD130694	14:50:17.1	-27:57:41.6	1.289	...	...
HD170642	18:32:21.0	-39:42:12.8	1.464	...	...
HD180928	19:18:59.6	-15:32:11.5	1.934	...	...
HD181342	19:21:03.9	-23:37:09.7	1.203	...	...
HD187111	19:48:39.3	-12:07:17.8	1.281	...	...
HD210049	22:08:22.8	-32:59:14.6	1.006	...	...
C2225316-145437	22:25:31.7	-14:54:39.6	1.033	...	...
J221821-183424	22:18:21.2	-18:34:28.3	1.026	...	...
J223504-152834	22:35:04.5	-15:28:34.9	1.047	...	...
J223811-104126	22:38:11.6	-10:41:29.4	1.218	...	...
C2306265-085103	23:06:26.6	-08:51:04.8	1.096	...	...
HD219615	23:17:10.7	+03:16:51.9	1.412	...	...

<sup>a</sup> S/N measured at 6000 Å for each target.

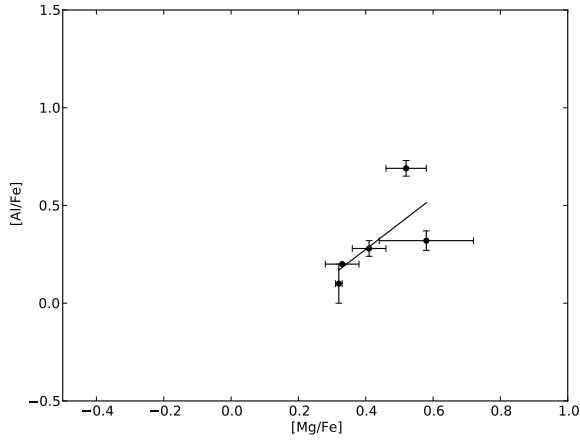


FIG. 4.— A plot showing  $[\text{Mg}/\text{Al}]$  for all Aquarius stream stars.

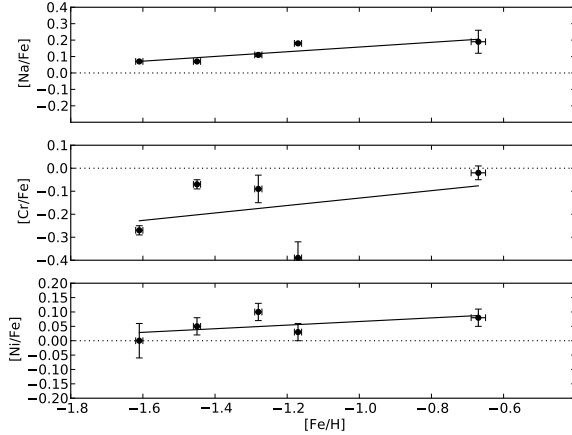


FIG. 5.— A plot showing  $[\text{Na}/\text{Fe}]$ ,  $[\text{Cr}/\text{Fe}]$ , and  $[\text{Ni}/\text{Fe}]$  for all Aquarius stream stars.

#### REFERENCES

- Asplund, M., Grevesse, N., Sauval, A. J., & Scott, P. 2009, ARA&A, 47, 481
- Bernstein, R., Shtetman, S. A., Gunnels, S. M., Mochacki, S., & Athey, A. E. 2003, in Society of Photo-Optical Instrumentation Engineers (SPIE) Conference Series, Vol. 4841, Society of Photo-Optical Instrumentation Engineers (SPIE) Conference Series, ed. M. Iye & A. F. M. Moorwood, 1694–1704



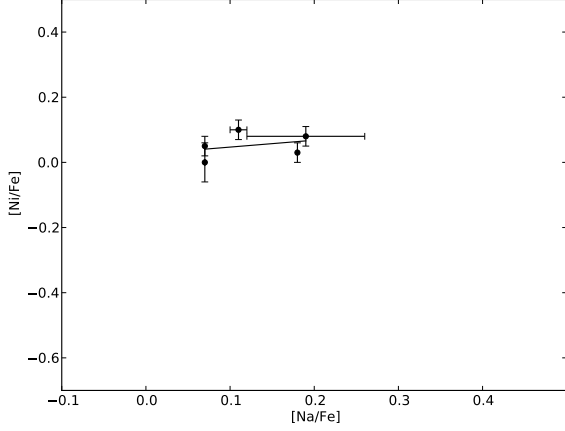


FIG. 6.— A plot showing  $[\text{Na}/\text{Fe}]$  and  $[\text{Ni}/\text{Fe}]$  for all Aquarius stream stars.

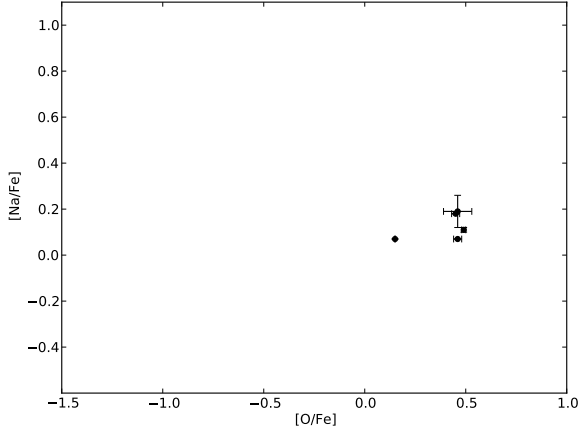


FIG. 7.— A plot showing  $[\text{O}/\text{Fe}]$  and  $[\text{Na}/\text{Fe}]$  for all Aquarius stream stars.

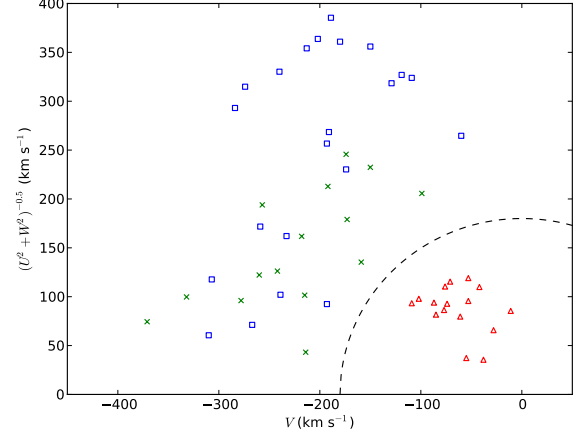


FIG. 8.— Toomre plot.

- Frebel, A., Simon, J. D., Geha, M., & Willman, B. 2010, *ApJ*, 708, 560  
 Fulbright, J. P. 2000, *AJ*, 120, 1841  
 Gratton, R. G., Sneden, C., Carretta, E., & Bragaglia, A. 2000, *A&A*, 354, 169  
 Grevesse, N., & Sauval, A. J. 1998, *Space Sci. Rev.*, 85, 161  
 Helmi, A., & White, S. D. M. 1999, *MNRAS*, 307, 495  
 Munari, U., Sordo, R., Castelli, F., & Zwitter, T. 2005, *A&A*, 442, 1127  
 Norris, J. E., Ryan, S. G., & Beers, T. C. 1996, *ApJS*, 107, 391  
 Reddy, B. E., Tomkin, J., Lambert, D. L., & Allende Prieto, C. 2003, *MNRAS*, 340, 304  
 Siebert, A., et al. 2011, *AJ*, 141, 187  
 Sneden, C. A. 1973, PhD thesis, The University of Texas at Austin.  
 Sobeck, J. S., et al. 2011, *AJ*, 141, 175  
 Steinmetz, M., et al. 2006, *AJ*, 132, 1645  
 Williams, M. E. K., et al. 2011, *ApJ*, 728, 102  
 Wylie-de Boer, E., Freeman, K., Williams, M., Steinmetz, M., Munari, U., & Keller, S. 2012, *ApJ*, 755, 35  
 Yong, D., Carney, B. W., & Teixeira de Almeida, M. L. 2005, *AJ*, 130, 597  
 Zwitter, T., et al. 2008, *AJ*, 136, 421